Title: Phase separation during ion exchange controls collapse and induces ordering in hydrated montmorillonite

Authors: Michael L. Whittaker, Sergio Carrero, Benjamin Gilbert, Jillian F. Banfield*

Contact: mwhittaker@lbl.gov

Phase separation during ion exchange controls collapse and induces ordering in hydrated montmorillonite

Michael L. Whittaker, Sergio Carrero, Benjamin Gilbert, Jillian F. Banfield*

Abstract

Aqueous ion exchange in clays plays a major role in water, nutrient, and contaminant storage and transport in soils, sediments, and clay suspensions. Here, we show evidence that interlayer collapse during ion exchange in montmorillonite proceeds via a process that resembles two-dimensional spinodal demixing, and that collapse promotes particle restructuring through delamination and restacking. By integrating low-dose cryogenic transmission electron microscopy and time-resolved X-ray scattering we observe that sodium is displaced from the interlayer of hydrated montmorillonite within a second after ion exchange with potassium, a poorly hydrated cation found to associate more closely with the silicate sheet surface. Two populations of homogeneously collapsed or un-collapsed particles form with no interstratification and with abundances that depend on the cation activity ratio in solution. Restacking of layers separated as a result of ion exchange produces particles that exhibit (near) crystallographic order from initially turbostratic stacking across two molecular layers of water.

1. Introduction

Clay minerals such as montmorillonite play an integral role in myriad natural processes involving H_2O, CO_2, nutrient, and contaminant transport and storage in soils, sediments, and clay-rich suspensions.[1] The dynamic behavior of montmorillonite arises from molecular scale interactions between 2:1 aluminosilicate layers, the counterions that balance charge arising from isomorphic substitutions within the layers, and associated waters of hydration (**Figure 1**). Varying the types and proportions of various interlayer species allows montmorillonite to expand and collapse reversibly,[2] leading to appreciable changes in the arrangements of particles composed of stacks of 2:1 layers.[3,4] These structural changes in turn control the rate of solute transport,[5] and dramatically affect rheological and/or mechanical properties of soils, sediments, and suspensions.[6,7]

Exchange of potassium for sodium in montmorillonite crystalline hydrates with either one, two, or three molecular layers of water separating the 2:1 layers has a well-known tendency to promote the collapse of swelling clays. This process is responsible for initiating the irreversible transformation of montmorillonite to illite, an anhydrous layer silicate. Illitization is a ubiquitous diagenetic reaction that can alter solute transport rates and reduce the storage capacity for interlayer H_2O and CO_2.[8] Initially turbostratic sodium montmorillonite subjected to repeated wetting and drying cycles in the presence of potassium develops mica-like crystallographic stacking order, proceeding through interlayered illite-smectite.[9]

Despite the importance of ion-exchange in clay-rich media we have only recently started to develop molecular-level understanding of the underlying mechanisms. Experimental and computational studies have established the critical role of water in the thermodynamics and kinetics of ion-exchange in smectites. Alkali cations with weaker hydration, such as potassium, are preferentially incorporated over more strongly hydrated ions such as sodium.[10-13] However, cation binding to the montmorillonite surface is endothermic,[14] and exchange is only exothermic overall when compensated by favorable cation hydration in solution.[15] Selectivity for poorly hydrated ions increases as the amount of interlayer water decreases, such that potassium can be stable in a two-water-layer hydrate but is not stable in a three-water-layer hydrate.[16] The presence of interlayer water also strongly affects ion-exchange rates, which are orders of magnitude slower in anhydrous phlogopites[17] and illites[18] than in hydrated smectites.[19]

A challenge for developing an improved understanding of ion exchange is that ion partitioning within smectite interlayers is directly coupled to layer swelling or collapse. To date, no computational or experimental approaches have been able to access the timescales over which these coupled dynamic processes act. Molecular dynamics simulations of montmorillonite swelling and collapse have produced free-energy relationships for a narrow range of conditions[7] but simulations are restricted to small system sizes and timescales. Experiments often probe equilibrium swelling states under a variety of conditions, but do not directly capture the rapid processes of swelling or collapse. There is also increasing appreciation that the mechanical properties of the 2:1 layers, and crystallographically-resolved details of their interactions,[20] are important. Yet, neither simulations nor experiments have been able to explore the impact of rotation, translation or bending of layers on ion exchange.

Here, we use time-resolved simultaneous small-, medium-, and wide-angle X-ray scattering (SAXS/MAXS/WAXS) to probe the dynamics of ion exchange upon rapid mixing of homoionic sodium- or potassium-montmorillonite suspensions with solutions containing the opposite cation. With a time-resolution of ~100 ms, we investigate the effects of ion exchange over three orders of spatial magnitude in reciprocal space. Transmission electron microscopy at cryogenic conditions (cryo-TEM) of hydrated samples *in aqua* provides a complementary snapshot of particle arrangements with at least 2.2 Å resolution in real space. Combined, these observations demonstrate that collapse is a phase transition that proceeds with small energy barriers accessible through thermal fluctuations. Physical separation of either collapsed or un-collapsed particles is achieved through delamination into smaller particles in the presence of potassium, enabling the development of stacking order that spans two molecular layers of water.

2. Results

2.1 Stopped-flow time-resolved X-ray scattering

Homoionic SWy-2 montomorillonite was resuspended in NaCl (1 M) or KCl (1 M) to a concentration of 20 mg/mL (herein called Na-MMT or K-MMT). SAXS/MAXS/WAXS were acquired simultaneously on three separate detectors[21] from both Na-MMT and K-MMT suspensions (**Figure 1a, d**), which served as a basis set of homoionic end-members for interpreting data from mixed-cation solutions. Comparable (020) + (110) peak intensities ($I_{K-MMT}^{(020)+(110)}/I_{Na-MMT}^{(020)+(110)} = 1.03$) and Porod invariants ($Q_{v,K-MMT}/Q_{v,Na-MMT} = 1.44$, **Materials and Methods**) between Na-MMT and K-MMT confirm that the nominally identical clay particle concentrations yielded very similar actual concentrations of suspended particles. However, the basal spacing peak intensity of K-MMT was much lower than the intensity of Na-MMT ($I_{K-MMT}^{(001)}/I_{Na-MMT}^{(001)} = 0.28$) and had much broader tails (**Figure 1, Supporting Table 1**). This indicates that there was a larger deviation from the average interlayer spacing in K-MMT and suggests that a higher fraction of the layers were poorly-stacked.

Higher order diffraction from the basal spacing peak was observed at $\ell \cdot q_{001}$, where ℓ is the diffraction order (ℓ = 2, 3, 4, and 6 for Na-MMT and n = 3, 5 for K-MMT). Integer values of ℓ are an indication that the interlayers are homogeneous and there is no interstratification. The very weak ℓ = even peaks in K-MMT are a result of potassium residing in close proximity to, or partially within, the silicate sheets. The presence of ℓ = 2, 3, 4 and 6 in Na-MMT suggests that sodium ions reside ~2.5 Å to either side of the interlayer midplane on average, in addition to positions similar to potassium near the silicate sheet, with varying occupancy and the absence of ℓ = 5 confirms the presence of iron in the octahedral sheet.[22] Electron density, ρ, profiles along the stacking direction were calculated by Fourier synthesis of the diffraction peak intensities[22] from MAXS data with SAXS and WAXS contributions subtracted (**Figure 1b, e**). These profiles are entirely consistent with intensity profiles measured directly from low-dose cryo-TEM images (discussed below) and are consistent with molecular models, which suggest that potassium makes inner-sphere complexes with ditrigonal cavities in the silicate sheet,[16,23] while the more tightly bound hydration shell of sodium increases its probability of residence near the interlayer midplane.[24-28]

Rapid mixing of Na-MMT with a separate solution of NaCl (1 M) had no measurable impact on scattering intensities at any length scale investigated (**Supporting Figure 2**). Invariance of the scattering in the SAXS region immediately after mixing, which is sensitive to the distribution of both the aqueous and clay phases,[4] suggests that mixing was complete before data acquisition commenced. Thus, any changes in scattering observed after mixing are the result of chemical processes due to ion exchange and not from turbulent flow or dilution of the montmorillonite particles.

Ion exchange was performed by mixing a KCl solution (1 M) with Na-MMT in four volume ratios; 2:1, 1:1, 1:2, and 1:3. This maintained a constant total ion concentration, thereby minimizing the effects of changing ionic strength on species activities. Cations compensating structural charge (~5-12 mM) represent less than 2% of the total concentration of each ion (between 250-667 mM) in the limiting case of complete exchange. Experiments were repeated at 5°C, 15°C, 25°C, and 35°C. Results were consistent across three repetitions at each condition (**Supporting Figure 3**) with the exception of 1:1 at 15°C and 1:2 at 25°C, for which only two separate experiments were conducted. Solutions with higher potassium concentrations exhibited lower overall intensity because the clay particle concentration was diluted to a greater extent, and because the X-ray absorption cross section of potassium is larger (**Supporting Information**).
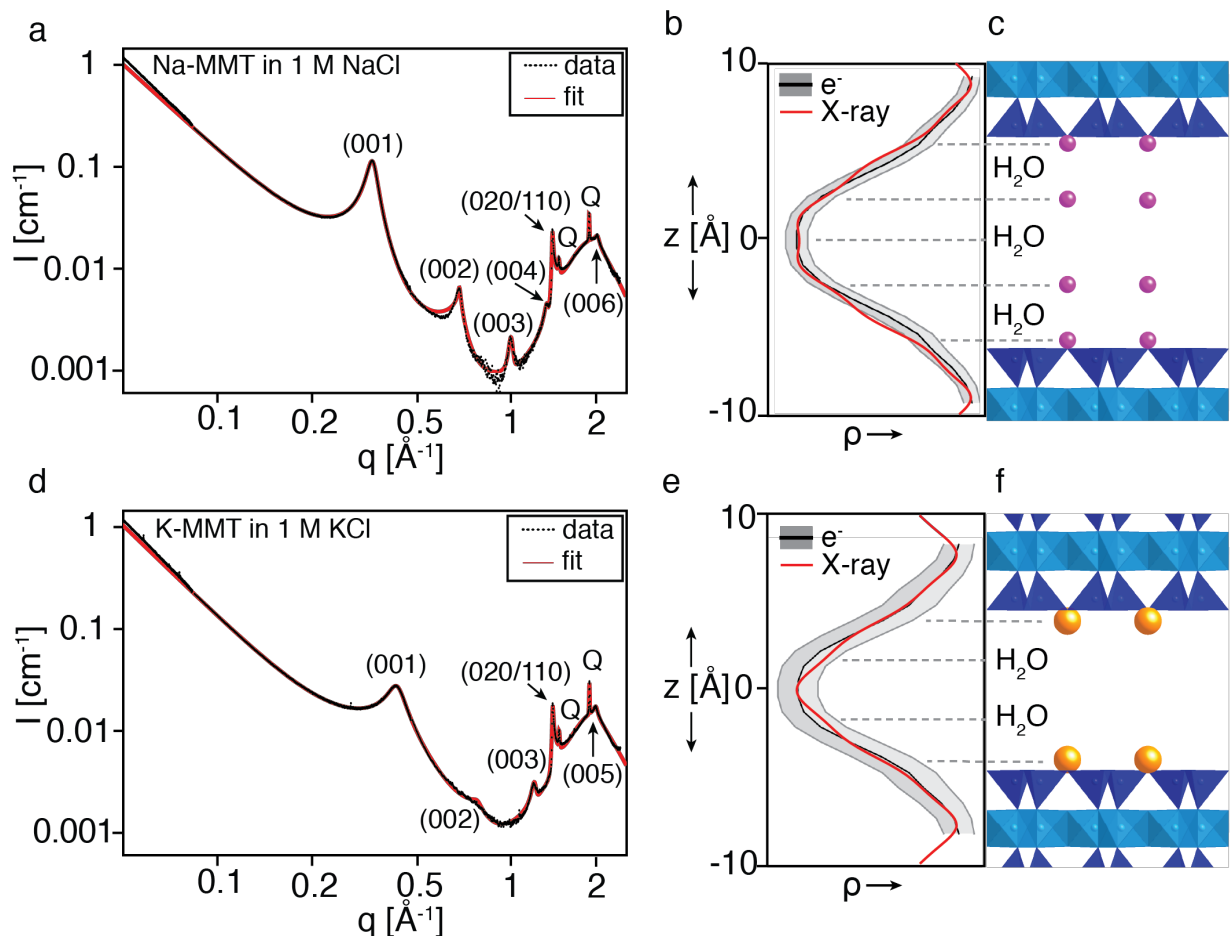
Figure 1. X-ray scattering from Na-MMT and K-MMT. (a, d) Whole-pattern SAXS/MAXS/WAXS fitting. (b, e) Electron density profiles calculated from MAXS diffraction peaks (red) or integrated TEM image contrast (black, one standard deviation in gray). (c, f) Atomic models depicting the structures inferred from the electron density profiles (interlayer water not explicitly shown).

Fits to the Na-MMT and K-MMT end-members (**Supporting Table 1**) served as an initial parameter set for the fitting of rapidly-mixed samples. Basal spacing peaks were broad (0.05 and 0.13 $Å^{-1}$ FWHM for Na-MMT and K-MMT, respectively) compared to the separation between the peak maxima (0.07 $Å^{-1}$) but under all conditions the Na-MMT peak at 19.0 Å decreased in intensity after mixing with KCl and a separate peak at 15.9 Å emerged (**Figure 2**). Fits to the data while allowing the peak location and shape parameters to vary confirmed that the positions of the primary basal spacing peaks did not change appreciably (**Figure 2a**). This is a strong indication that the collapse front within an interlayer region is sharp and/or moves rapidly on the timescale of the measurements (~50 ms acquisition time). A single broadened peak with a maximum between the homoionic end members was not observed under any *in situ* conditions in this study, but is observed in partially dried samples (**Supporting Figure 1**). This excludes the possibility of extensive interstratification of collapsed and un-collapsed interlayers *in situ*,[29] which is directly supported by cryo-TEM observations (below).

In Na-MMT, the $\ell = 2$ intensity was approximately 4% of the $\ell = 1$ intensity at equilibrium (**Supporting Table 1**). The total noise level in the $\ell = 2$ region ($0.56 < q < 0.76$ $Å^{-1}$) after mixing was far less (by a factor of 2.7 - 9.6) than the intensity expected in this region by taking 4% of the 19 Å peak intensity (**Supporting Table 2**), such that this peak would be resolved if present for all but the highest mixing ratios and temperatures. Weak intensity in this region that fades after the first acquisition was often observed in such cases (e.g., **Figure 2a**), even when collapse did not go to completion.
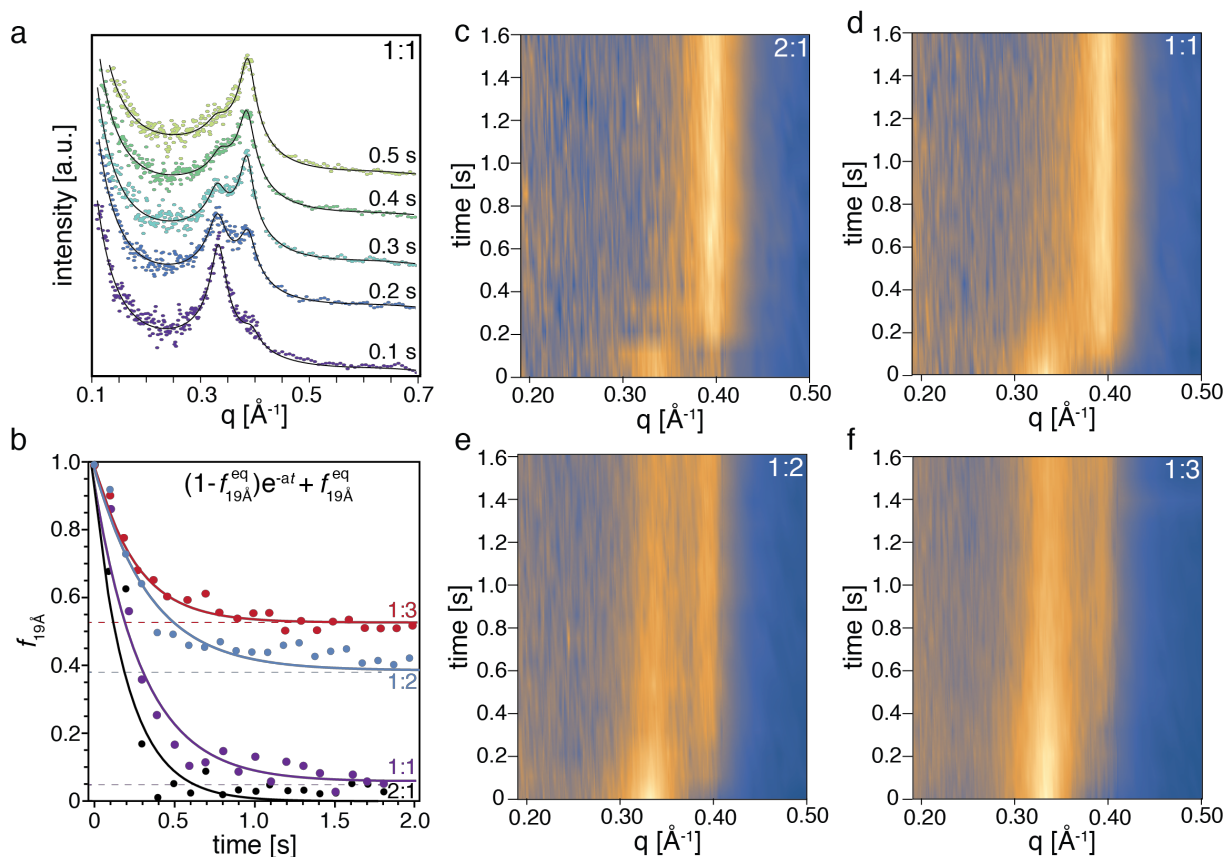
Figure 2. Collapse dynamics during ion exchange between KCl (1 M) and Na-MMT. (a) 1:1 solution ratio at 5°C, showing the emergence of a 2-layer hydrate peak at $q = 0.395$ Å^{-1} (15.9 Å) immediately following mixing. (b) Time dependence of the extent of collapse, $f_{19\,\text{Å}}$, for representative data from four KCl:Na-MMT mixing ratios. (c-f) Plots of total scattering intensity in the basal spacing region ($q = 0.2$-0.5 Å^{-1}) during the first 1.6 seconds after mixing with different ratios of K:Na-MMT (values indicated top right).
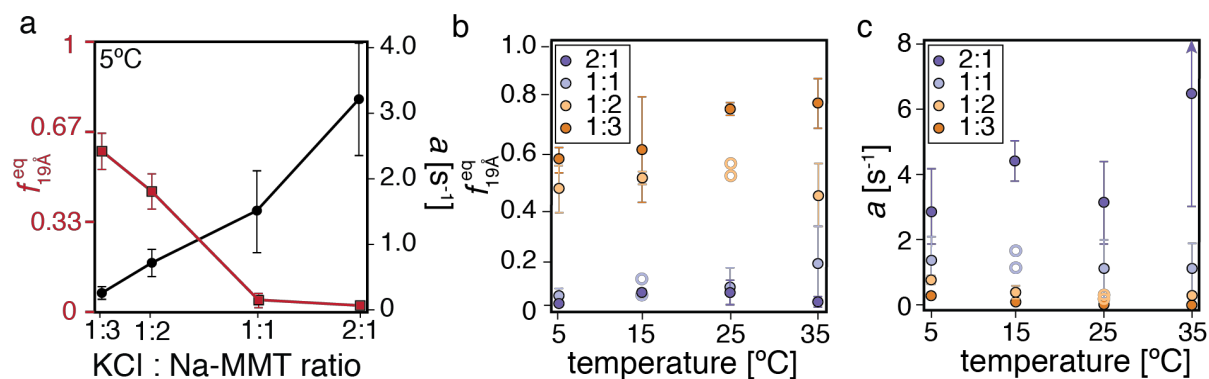
Figure 3. Potassium concentration and temperature dependence of $f_{19\,\text{Å}}^{eq}$ and a. (a) The collapse rate constant increases approximately linearly with mixing ratio, while $f_{19\,\text{Å}}^{eq}$ decreases approximately linearly to a ratio of 1:1, at which point collapse goes to near-completion. (b, c) No strong temperature dependence was observed for either $f_{19\,\text{Å}}^{eq}$ or a. Error bars represent one standard deviation of three measurements. Open circles represent individual measurements from conditions at which only two data points were collected.

Integrated intensity from both basal spacing peaks, expressed as the fraction of 19 Å hydrate, $f_{19\,\text{Å}} = I_{Na-MMT}^{(001)} / (I_{K-MMT}^{(001)} + I_{Na-MMT}^{(001)})$, was used to quantify the collapse rate (**Figure 2b**). The total intensity from both peaks ($I_{K-MMT}^{(001)} + I_{Na-MMT}^{(001)}$) decreases (**Figure 2c-f**), which requires that the total coherent scattering volume decreases as collapse progresses. But the (020) + (110) peak intensity and Porod invariant remain constant, indicating that the particle concentration does not change and therefore that particles must rearrange into configurations that diffract less strongly during collapse.

A regime of apparent equilibrium followed collapse, in which the peak intensities did not change appreciably (**Figure 2c-f**). The fraction of the 19 Å peak intensity in this regime, $f_{19\,\text{Å}}^{eq}$, was used to quantify the extent of collapse. At KCl:Na-MMT ratios of 2:1 and 1:1, $f_{19\,\text{Å}}^{eq}$ was close to zero after two seconds, representing nearly complete collapse of all particles (**Figure 2b, c, d**). At lower mixing ratios (1:2 and 1:3) both peaks coexisted and approached an $f_{19\,\text{Å}}^{eq}$ greater than zero (**Figure 2b, e, f**).

A decaying exponential that accounts for the variable $f_{19\,\text{Å}}^{eq}$ was fit to all collapse rate data with a single rate constant, a (**Figure 2b and Equation 4, Materials and Methods**). Both $f_{19\,\text{Å}}^{eq}$ and a were strong functions of the potassium concentration. At 5°C, $f_{19\,\text{Å}}^{eq}$ decreased approximately linearly up to a KCl:Na-MMT ratio of 1:1, at which point collapse proceeded to near-completion. Over the same range of KCl:Na-MMT ratio a increased linearly (**Figure 3a**). Neither $f_{19\,\text{Å}}^{eq}$ nor a exhibited a strong temperature dependence (**Figure 3b, c**). Between 5°C and 35°C $f_{19\,\text{Å}}^{eq}$ increased from 0.59 to 0.77 at the lowest ratio of 1:3, but was not strongly affected at higher potassium content. At the highest potassium concentration ratio of 2:1 the uncertainty in a was significant due to lower signal to noise from both dilution of MMT particles and stronger X-ray absorption from potassium, as well as collapse that was already in progress before the first measurement (within ~30 ms). Nonetheless, a did not exhibit a strong temperature dependence at any mixing ratio. This behavior contrasts with ion diffusion-limited exchange in anhydrous phyllosilicates,[17] which increases appreciably with temperature through the Arrhenius behavior of the diffusion coefficient.[30] Interlayer water diffusion has a strong temperature dependence,[31] and partitioning between bulk solution and the interlayer is essentially barrierless,[32] indicating that neither process limits collapse.

3.2 Low-dose cryo-TEM

Low-dose cryo-TEM imaging was employed to directly examine particles of SWy-2 *in aqua* after cryo-freezing. Rapidly quenched 1:2 KCl:Na-MMT mixtures (**Figure 4**) were compared to Na-MMT and K-MMT end-members (**Figure 5**). With spatial resolution of ~2 Å, both the interlayer spacing and intralayer lattice fringes were used to characterize three-dimensional layer orientations and particle arrangements from two-dimensional images. Basal spacing measurements were obtained directly from real-space images as described for osmotic hydrates.[33] However, persistent defects introduced significant error when layers were not well-stacked (**Figure 4c**). Additionally, integrated Fourier transform (FT) profiles (**Figure 4d**) were used to quantify the distribution of interlayer spacings within whole images or image sub-regions (**Materials and Methods**). Na-MMT exhibited predominantly 19.3 ± 2.1 Å interlayer spacings, while K-MMT exhibited 16.4 ± 2.5 Å spacings in integrated FT profiles (**Figure 4e**). Larger interlayer spacings are expected for samples frozen at cryogenic temperatures compared to aqueous samples at ambient conditions due to the expansion of vitreous ice,[34] which accounts for differences between cryo-TEM and X-ray scattering data. Despite these small differences, contrast profiles measured parallel to the stacking direction were highly consistent with the electron density profiles calculated from X-ray scattering basal spacing peak intensities (**Figure 1b, e**).

While 2:1 and 1:1 mixing ratios underwent complete collapse too rapidly for the cryo freezing procedure to quench the reaction, the finite $f_{19\,\text{Å}}^{eq}$ at 1:2 KCl:Na-MMT, with appreciable amounts of both collapsed and un-collapsed interlayers, made this composition amenable to characterization via cryo-TEM. Two distinct populations of particles exhibited either ~16 Å or ~19 Å interlayer spacings (**Figure 4e**).

Average interlayer spacings were determined from integrated FTs from 8 different particles comprising a total of 81 layers. Two particles (30 layers) retained ~19 Å spacing, while 6 particles (51 layers) were collapsed and had an average of ~16 Å interlayer spacing. The fraction of collapsed layers (30/81 = 37%) is comparable to $f_{19\,\text{Å}}^{eq}$ at this composition measured from X-ray scattering (48 ± 8%, **Figure 2b**). Given the high fidelity for all edge-on layers in cryo-TEM, and the under-representation of K-MMT from X-ray scattering on a per-layer basis, this constitutes good agreement for $f_{19\,\text{Å}}^{eq}$ between the two techniques, and confirms that two populations of non-interstratified particles with different average basal spacings co-exist.

The number of layers per particle for Na-MMT (mean ± one standard deviation = 7.4 ± 4.8, N = 982 layers from 133 particles) and K-MMT (7.2 ± 6.1, N = 708 layers from 98 particles) were distributed lognormally (**Figure 4f**). The distribution of K-MMT particle sizes exhibited a higher skewness, resulting in a modal layer number per particle (2.5) smaller than that of Na-MMT (4.4). Individual layer areas vary over four orders of magnitude (also distributed lognormally) and have irregular shapes (**Supporting Figure 4**). Due to the large variability in layer dimensions, all MMT particles were incompletely stacked and defective. Defects frequently consisted of layers that terminated within a stack or layers that extended past the edge of neighboring layers. The former manifests as the asymmetric broadening observed on the high q side of basal spacing peaks. The latter is captured in the lower modal layer number for K-MMT, which results in a larger fraction of the total layer volume that is not stacked in a coherently diffracting domain and is consistent with the lower basal spacing peak intensity for the same layer concentration (**Figure 1**).
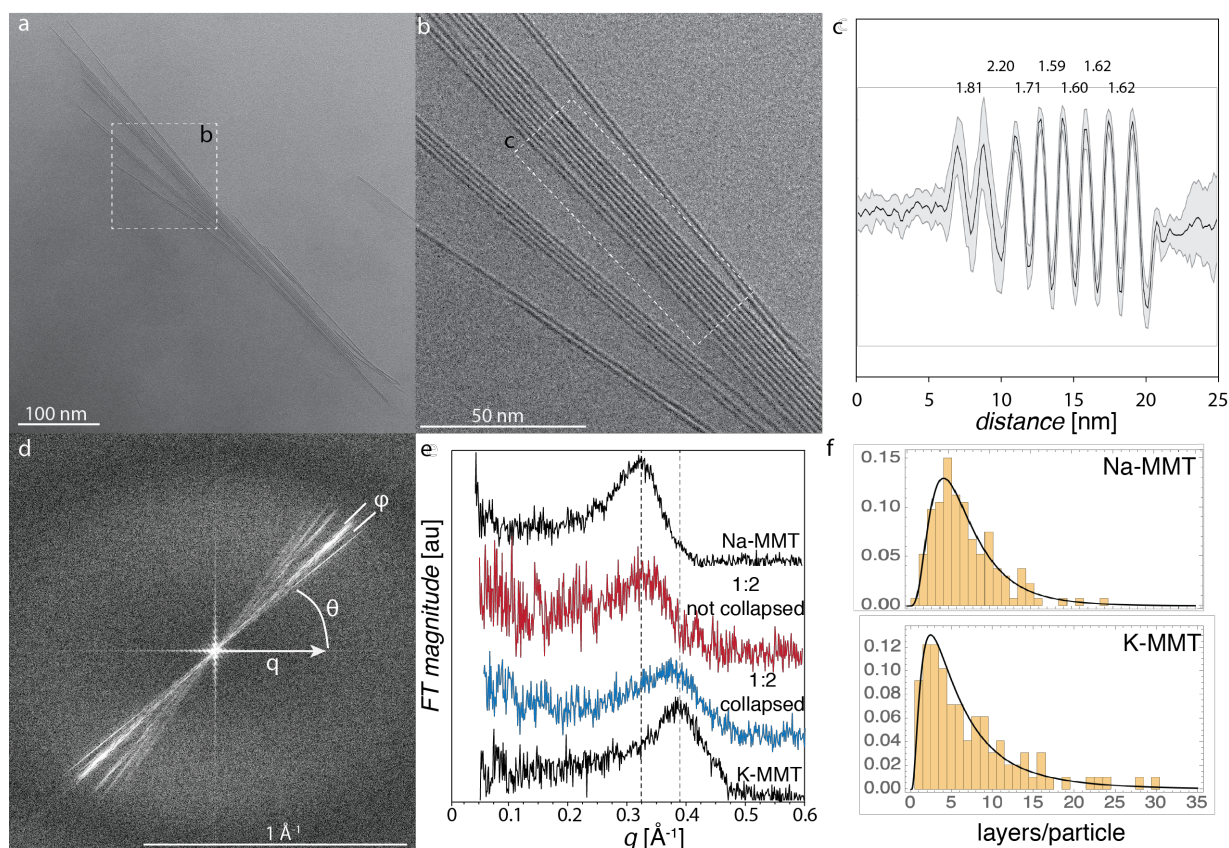
Figure 4. Cryo-TEM of 1:2 KCl:Na-MMT. (a) Low magnification image of particle. (b) Higher magnification of region indicated in (a), showing at four distinct stacking orientations from the same 'particle' comprising 16-20 layers. (c) Average intensity (one standard deviation in gray) integrated along the region indicated in (b). (d) FT of (a) (e) Comparison of the FT magnitude integrated along q for a given angular range φ for Na-MMT, K-MMT, and either collapsed or uncollapsed particles in the 1:2 sample. (f) Histograms of number of layers per particle for Na-MMT and K-MMT.

Particles in 1:2 KCl:Na-MMT mixtures exhibited multiple 'sub-particles' consisting of more than one layer not in contact with adjacent layers along their entire length (**Figure 4a, b**). This, along with decreasing total basal spacing intensity in X-ray scattering during collapse, is an indication that particles undergo partial delamination as a consequence of the ion exchange process, reducing both the average number of layers per particle and the total coherent scattering volume. Na-MMT particles were mostly coplanar, even preserving their spacing across gently deformed regions (**Supporting Figure 5**), while K-MMT layers were often twisted, bent and frequently exhibited a distribution of orientations in a disordered aggregate (**Figure 5a, d**).

Layers that were oriented edge-on with respect to the beam direction were rarely also aligned along a high-symmetry zone axis. Layers not aligned along a zone axis have no appreciable contrast variation within the layer and appear uniformly dark (**Figure 5a, c**). However, lattice fringes were frequently observed in regions directly adjacent to an edge-on particle, and FT of this region revealed in-plane lattice spacings of 2.2-2.3 Å and 4.5-4.6 Å, consistent with the (040)/(220)/($\bar{2}$20) and (020)/(110)/($\bar{1}$10) lattice planes, respectively, of individual clay layers (**Figure 5**). Bragg filtering of the FT by retaining only intensity associated with the spot(s) of interest, and taking the inverse FT, was used to correlate face-on lattice fringes with edge-on particles from a single image (**Supporting Figure 6**). Lattice spacings in the FT of three Na-MMT layers were found to be separated by 8 and 13° (**Figure 5b**) and Bragg-filtering confirmed that they originate from the same layers viewed edge-on. This is consistent with turbostratic stacking commonly observed for montmorillonite.[35] A fourth FT spot is identified from the Bragg filtered-FT as coming from a separate part of the image region and is not directly associated with the three-particle stack.
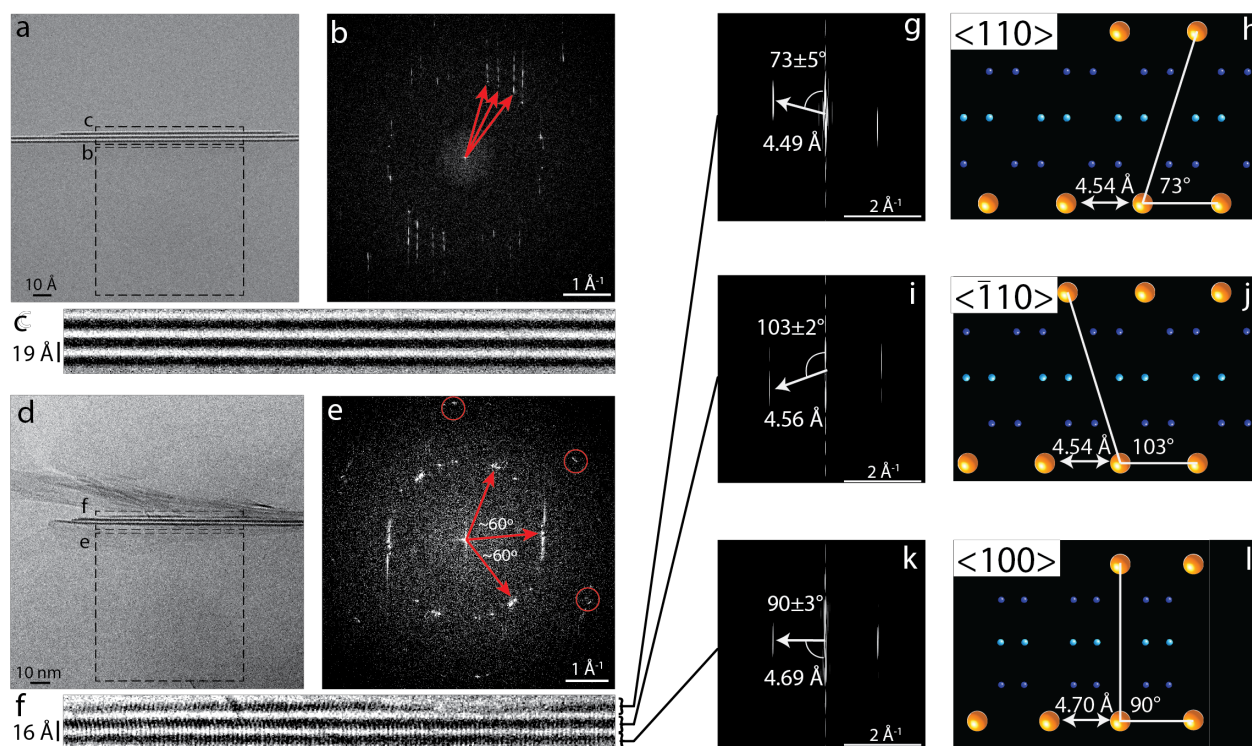
Figure 5. Cryo-TEM of Na-MMT and K-MMT. (a) Low-dose high resolution cryo-TEM image of a curved Na-MMT particle consisting of three layers, part of which is viewed edge-on. None of the layers are oriented along a high-symmetry zone axis, but their orientation could still be determined from the FT of the adjacent region of the particle viewed face-on (b). Arrows indicate FT spots from distinct layers that are separated by 8° and 13° relative to each other. (c) No cross fringes are evident within the layers. (d) K-MMT particle, with three layers that are oriented edge on and many others in undetermined orientations. (e) FT spots associated with edge-on particle are clustered in ~60° intervals, while spots from other layers are randomly oriented. Higher order spots (circled), which are only visible for

layers oriented close to face-on, confirm these relative orientations. (f) Cross fringes indicate that all three layers are in distinct orientations. (g) – (l) Fourier transform of the top, middle and bottom layer in (f), showing streaks corresponding to the projected potentials along different zone axes. The data indicate the top layer is viewed down <110>, the middle down <$\bar{1}$10> and the bottom down <100>.

By chance, some Na-MMT layers were oriented along a high-symmetry axis (**Supporting Figure 7**). However, these layers had no special orientational relationship with their neighbors. In contrast, some K-MMT particles exhibited intra-particle lattice fringes that maintained correlated orientations across multiple neighboring layers (**Figure 5d, f**). For example, lattice spacings from individual layers could be resolved in three adjacent layers in the same K-MMT particle in **Figure 5d-l**. Fourier transformation of a narrow region containing only a single layer (**Figure 5f**) revealed the average spacing and angular orientation of each set of fringes (**Figure 5g, i, k**). Based on the angle at which the expected atomic potentials make when viewed edge-on,[36] each layer was uniquely attributed to <100>, <110> or <$\bar{1}$10> zone axes. With direct knowledge of the orientation of each layer viewed edge-on, the FT of the face-on orientation confirms that lattice spots associated with these particles were clustered at ~60° intervals, as expected from the lattice constants of individual layers (**Figure 5e**).

3. Discussion

These data paint a clear picture of collapse that proceeds through phase separation, resulting in particles that are non-interstratified and chemically homogeneous. This extends previous observations of phase separation between two distinct interlayer structural states[11,37-39] to the case of ion exchange that is coupled to clay swelling and collapse. We provide direct evidence that layers can delaminate after potassium is introduced, as previously inferred from light transmission measurements in analogous cation exchange reactions,[40,41] and suggest that this provides a mechanism for the spatial segregation of different collapse states as well as the rotation and re-attachment at (near) crystallographic orientations via Brownian motion.

Consideration of the relative stabilities of the two- and three-water-layer hydrates and the preference of these two interlayer structures for either potassium or sodium is key to understanding the process of phase separation in K/Na–MMT. The observed end-member structures, with sodium in three-water-layer hydrates residing more often near the interlayer midplane and potassium in two-water-layer hydrates making inner-sphere coordination with MMT layers, correspond to local minima in free energy.[15,16,42-44] Cation hydration energies are the most significant contributions to the difference.[42,45] For a general solution composition, the water activity is in equilibrium with neither of these states but with a non-integer amount of interlayer water. In mixed-cation systems with different hydration energies, this allows for the possibility of two coexisting basal spacings in equilibrium that are lower in energy than the mixed-cation single phase. The coexistence of potassium-rich two-water-layer interlayers and sodium-rich three-water-layer interlayers adheres to Gibbs' phase rule (**Supporting Figure 8**). Similar behavior has been observed in mixed cation solutions,[46] although was not described in the context of phase separation. The coexistence of MMT phases with different hydration states under varying relative humidity is frequently observed in MMT systems,[47-50] including here (**Supporting Figure 1**), but is typically ascribed to natural variability in layer charge rather than spontaneous phase separation.

In summary, we infer that phase-separated two- and three-water-layer interlayers are in dynamic equilibrium at an abundance (i.e., $f_{19\,\text{Å}}^{eq}$) that is determined by the cation ratio in solution and the water potential which, in the present system, is determined by the ion concentration (1 M) and identity. Thus, the fraction of collapsed and un-collapsed layers, as well as their compositions, are fixed by the aqueous phase. This model is incomplete, however, without a mechanistic description of the feedback between ion exchange and collapse and the observed structural rearrangement of collapsed particles.

A striking finding of this work is layer collapse is significantly slower than the replacement of potassium for sodium by diffusion within the interlayer. We constructed a continuum model of potassium diffusion at a 1:1 mixing ratio using the measured layer size distribution, which shows that complete intercalation is expected to occur in less than a millisecond (**Supporting Figure 4**). In addition, disappearance of $\ell = 2$ diffraction intensity in all samples after mixing confirms that potassium intercalated within the interlayer before collapse initiated. Particles therefore exist in a mixed-ion configuration that is unstable with respect to phase-separated interlayers prior to collapse. That $f_{19\,\text{Å}}$ takes three orders of magnitude longer to reach an apparent equilibrium indicates that additional phenomena must be required to initiate interlayer collapse.

We propose that demixing within the interlayer is the first step in the process of collapse, and is promoted through positive feedback between the local chemical composition and the interlayer spacing. Regions that become enriched with potassium exhibit weaker hydration that promotes the recruitment of more potassium, and the opposite is true of sodium.[10,11] Both $f_{19\,\text{Å}}^{eq}$ and a are largely invariant with temperature, which is consistent with the non-Arrhenian cation diffusion previously observed for MMT,[31,51] but inconsistent with most other processes likely to limit collapse. Thus, diffusional separation of sodium and potassium within the interlayer are required to initiate collapse.

Dynamic fluctuations within the interlayer, in which the composition, hydration state, and basal spacing are all tightly coupled, must be common and an important aspect of ion-driven swelling and collapse. Differences in hydration energy between two- and three-water-layer hydrates are 0-4 kT/unit cell of clay, with barriers of comparable size in between,[15,16,42-44] suggesting that both states are regularly

explored in fluctuations from the average basal spacing. These fluctuations may present continually changing migration barriers analogous to those responsible for non-Arrhenian behavior in ion conducting polymers.[52] Therefore, fluctuations leading to a potassium-rich region may also contribute to the initiation of collapse. Specifically, both X-ray scattering peaks and integrated FT profiles of Na-MMT have little intensity below the K-MMT peak maximum at $q = 0.40 \, Å^{-1}$. However, K-MMT particles regularly exist at 19 Å, contributing to much broader X-ray scattering and integrated FT peaks. Direct measurements of interlayer spacings (**Figure 4 b,c**) exhibit standard deviations of approximately 15%, or 2-3 Å, consistent with regular exploration of both hydration states with a barrier of ~2 kT between them.

  Because potassium-saturated three-water-layer hydrates are unstable under any conditions,[16,42] a potassium-rich region spanning both sides of the interlayer that reaches some critical size will expel a layer of water, dramatically accelerating the recruitment of more potassium and expulsion of sodium to complete the collapse of the entire interlayer. This critical size could not be determined quantitatively here, but the concentration dependence of both $f_{19\,Å}^{eq}$ and a point to its existence. Extrapolating the linear increase in $f_{19\,Å}^{eq}$ with decreasing potassium content below 1:1 mixing ratio in **Figure 3a** to unity gives a potassium fraction that is larger than that at which a approaches zero. In the range of concentrations between these two values collapse is thermodynamically favored but proceeds very slowly, i.e., swelling/collapse hysteresis. This is because there is not sufficient potassium within an un-collapsed interlayer to produce potassium-rich regions that can sustain collapse via the recruitment of more potassium before fluctuations dissipate the potassium, introduce sodium, or alter the hydration state to un-collapse the region.

  Based on the foregoing evidence, we propose a model of collapse outlined in **Figure 6**. Ion intercalation into initially homoionic Na-MMT (**Figure 6a-b**) is rapid but collapse is not immediate (**Figure 6c-d**). As the composition in the interlayer equilibrates with the surrounding solution, potassium diffuses throughout the basal surface of the MMT layer, and collapse is initiated by demixing within an interlayer. Demixing promotes potassium colocalization across both sides of an interlayer (**Figure 6e-f**), eventually reaching a sufficient size to overcome fluctuations and initiate collapse. Once an interlayer collapses, neighboring layers can in some cases be liberated through delamination, and may then rotate into preferred rotational configurations via Brownian motion (**Figure 6g-h**).

  MMT layers can stack with mica-like crystallographic order at relative orientations of only 0 or 180° degrees. However, at relative particle rotations of ~60°, neighboring particles can come into near-crystallographic alignment along the <110>, <$\bar{1}$10>, <100> directions. It has long been known that in the initial steps of illitization mica-like stacking order develops after repeated wetting and drying cycles in the presence of potassium[9] resulting in this type of near-crystallographic ordering.[8] This is the first demonstration that the emergence of this order first arises in suspension as a result of phase separation following potassium exchange, and is maintained across up to 6 Å of water. Bending moduli of individual clay layers vary with crystallographic orientation,[20] and thus, (nearly)-oriented layers are expected to be more rigid and less susceptible to perturbations through fluctuations, preserving their relative orientations.
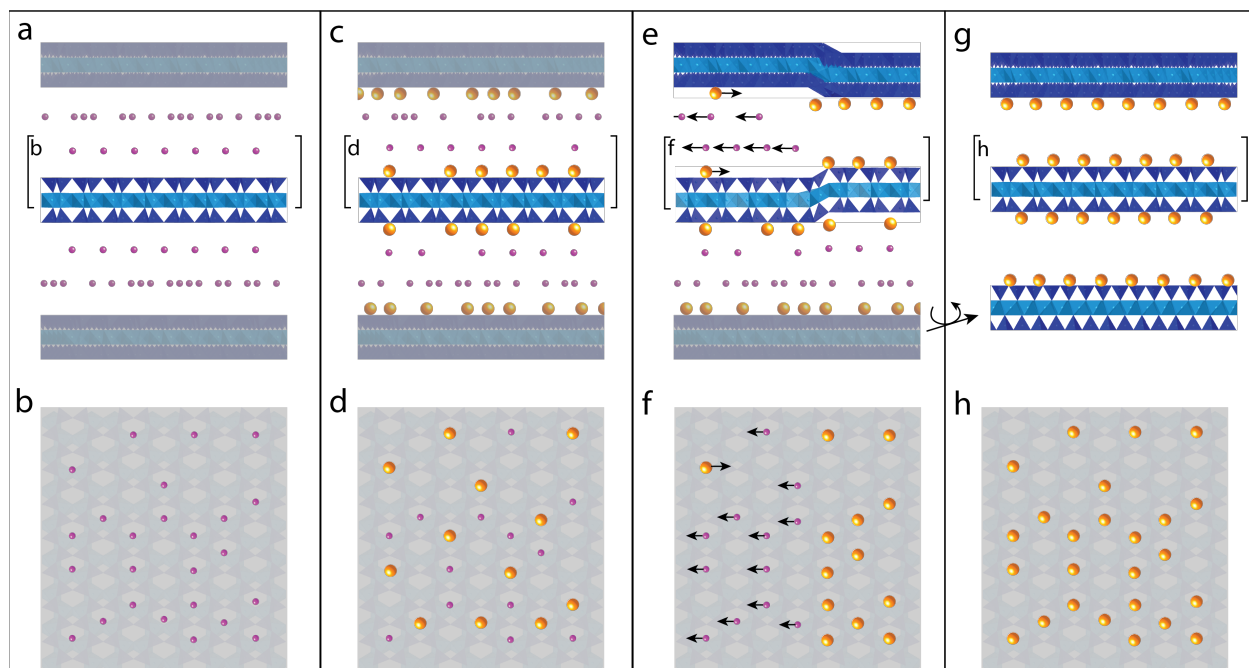
Figure 6. Model of ion exchange and collapse. (a) Edge-on view of initial turbostratic stacking of three layers in Na-MMT. (b) Hypothetical distribution of sodium in proximity to the top of the middle layer, viewed face-on. (c-d) Exchange of potassium for sodium that proceeds prior to collapse. (e-f) Partial collapse induced by critical local potassium concentration. (g-h) Collapse propagates throughout layer, expelling sodium and a single layer of water. Neighboring layer becomes delaminated, allowing it to rotate into more favorable configuration.

4. Conclusions

Potassium exchange for sodium in montmorillonite initiates via a process resembling spinodal demixing within the interlayer. Delamination into particles with fewer layers during collapse produces two coexisting populations of collapsed or un-collapsed particles that are chemically and physically separated. Strongly coupled fluctuations in the composition, hydration, and basal spacing, likely play a key role in initiating collapse and controlling its extent. This process is a demonstration of the nanoscale chemical-mechanical coupling that controls the rate and products of ion exchange and the structures that result from collapse in hydrated montmorillonite.

This new understanding of exchange equilibria in which multiple swelling states are present will improve the predictive capacity of exchange models of ion binding in swelling clays. It also provides a framework for interpreting ion adsorption in multicomponent systems. For example, these results suggest that interlayered illite-smectite may be a kinetically trapped metastable phase. Clay-rich systems for which ion exchange cannot go to completion due to, e.g. stearic hinderance of rotational degrees of freedom, must therefore have residual excess free energies due to unresolved swelling pressures and compositional heterogeneity. These energies may be difficult to predict *a priori* using currently available modelling techniques, but may be quantifiable nonetheless. By imaging clay suspensions *in situ* with high throughput, the probabilities of varies configurational states allows for the direct measurement of energy landscapes.

5. Experimental Procedure

Materials

Wyoming montmorillonite (SWy-2), obtained from the Source Clays Repository of The Clay Minerals Society, was used throughout this study. An aqueous diluent phase, (herein called clay-saturated aqueous phase, CSAP) saturated with respect to SWy-2, was made by dialyzing SWy-2 (10 mg) against MilliQ water (1 L, resistivity > 18.2 MΩ·cm) for 1 week and filtering through a 0.02 μm filter (Whatman). Aqueous solutions of NaCl and KCl were prepared from reagent-grade salts and CSAP to ensure that solutions were equilibrated with respect to the clay to avoid artifacts from dissolution.

Clay Treatment

To obtain homoionic montmorillonite, SWy-2 (2-10 g) was dispersed in NaCl or KCl (1 M, 50 mL made from CSAP) in a polypropylene bottle (50 or 1000 mL) and mixed on a rotating mixer (5 rpm) for seven days. Sedimentation of coarse particles was achieved by centrifugation (1000 rcf for 10 minutes). Fine particles were separated from the coarse sediment and transferred to a cellulose dialysis membrane (Spectra/Por 3, 3.5 kDa molecular weight cutoff). Excess salt in the supernatant was removed by dialysis against CSAP, which was replaced every day for seven days. The resulting clay gel was dried in a convection oven (60°C for 14 hours, then 110°C for 6 hours). Suspensions were prepared by redispersing homoionic powder in either NaCl (1 M) or KCl (1 M) to a final concentration of 2% by weight and sonicating in an ultrasonic bath at 45°C for 24 hours. Herein, we will refer to these suspensions as 'Na-MMT' or 'K-MMT'.

Time-resolved X-ray scattering

X-ray scattering was performed at beamline 5ID-D of the Advanced Photon Source at Argonne National Laboratory. Small-, medium-, and wide-angle X-ray scattering (SAXS/MAXS/WAXS) was collected simultaneously on three Rayonix charge-coupled device (CCD) detectors with sample−detector distances of 8505.0, 1012.1, and 199.5 mm, respectively. Sample-detector distances, orientations, and diffraction line broadening were calibrated using a silicon grating (7200 gr/mm), silver behenate, and lanthanum hexaboride standards, respectively, and the absolute intensity was calibrated with a glassy carbon standard. The wavelength of radiation was set to 1.2398 Å (10 keV), resulting in a range of scattering vector, $q = 0.017−4.2$ Å^{-1}. Two dimensional scattering patterns were corrected for varying incident beam intensity and sample transmission with a CdWO$_4$ diode and azimuthally averaged using GSAS-II.[53,54] Absolute scattering intensity, $I(q)$, of the clay suspensions was obtained by subtracting the average of 50 frames acquired from MilliQ water and the quartz capillary (1.0 cm outer diameter) from each scattering pattern.

Time-resolved acquisition was enabled by a stopped-flow mixing device (Biologic SFM400, controlled with Bio-kine software). Flow rates between 1-2 mL/s for mixing 250-500 μL of solution through Berger-Ball mixers resulted in dead times between 18.3-36.6 ms, representing a transient mixing stage. Exposure times of 0.5 s at 1 s intervals (2x2 pixel binning) or 0.025 s at 0.050 s intervals (6x6 pixel binning) set the minimum time resolution during the stopped-flow stage. Turbulent flow of these small volumes was confirmed to yield perfect mixing during the transient stage (before the start of data acquisition) by comparing the absolute scattering intensity from MilliQ water, 1 M KCl, and mixtures of these two solutions in 2:1, 1:1, 1:2 ratios. Following each measurement, the sample was cleared from the capillary with five volumes of water (~ 0.5-1 mL), and the capillary was cleaned with five volumes of water, five volumes of alcohol, and dried with air in between samples. Each experiment was repeated three times, and the results were reproducible across each run.

The (020) and (110) reflections in the WAXS region ($q = 1–4.5$ Å^{-1}) confirmed the presence of montmorillonite as well as residual quartz that was used as an internal calibration standard. In the SAXS region ($q < 0.1$ Å^{-1}) a Porod slope of ~3 was the dominant feature. The MAXS region ($1.5 > q > 0.1$ Å^{-1}) was characterized by the presence of a strong diffraction peak at $q_{001} = 0.331$ Å^{-1} (19.0 Å) for Na-MMT and $q_{001} = 0.398$ Å^{-1} (15.9 Å) for K-MMT, characteristic of 3- or 2-water layer crystalline hydrates,

respectively. Scattering data were fit with an in-house code written in Mathematica. A Gunier-Porod fit in the SAXS region, three (K-MMT) or five (Na-MMT) (00ℓ) basal spacing peaks, Bragg peaks corresponding to the (020) and (110) MMT lattice planes and quartz (Q), and two broad Gaussains for diffuse WAXS scattering were required for a comprehensive fit to the X-ray scattering data. Fitting in the SAXS region was performed using a modified Guinier-Porod model[55] for thin platelets where the scattering intensity I at scattering vector $q = 4\pi sin(\theta)/\lambda$, takes the form

$$I(q \ll 1) = Ae^{-\frac{(qR_g)^2}{3}}q^{-P} \qquad (1)$$

where A is a pre-exponential intensity factor for the particle radius of gyration R_g and P is the Porod slope. The radius of gyration, R_g, defined as $R_g^2 = 3/2R^2$, was fixed at 560 Å based on the average particle radius calculated from AFM measurements of the particle size distribution (**Supporting Figure 7**). A Porod slope of $P = -2.85$ for Na-MMT and -2.93 for K-MMT low q (**Supporting Table 1**) is characteristic of lamellar structures separated by interlayer water,[4] with K-MMT slightly denser, as expected for a smaller basal spacing.

Non-negligible peak asymmetry to the low-q side of the basal spacing peak has been frequently observed previously,[56,57] but has been attributed primarily to Scherrer-type broadening. Cryo-TEM images confirm that defects, primarily the termination of layers within a stack, give rise to spacings that are larger than the average interlayer separation in the vicinity of the termination (**Supporting Figure 8**). Radially integrated FT magnitudes from cryo-TEM images are in excellent agreement with X-ray profiles. Here, we introduce a new peak profile function that was employed to fit the basal spacing peaks and higher order reflections. This function was necessary to fit the very broad tails of the peak profiles of both potassium- and sodium-saturated montmorillonite and low-q asymmetry due to defective stacking motifs measured in cryo-TEM. The diffraction intensity, I, in the vicinity of a diffraction peak at q_d is given by

$$I(q) = C\left[1 + \frac{(q-\mu)^2}{\sigma*\left(\frac{2\gamma}{1+e^{\alpha(q-\mu)}}\right)^2}\right]^{-\sigma} \qquad (2)$$

were μ is the peak position, σ determines the extent of the tails, γ is a shape parameter, α defines the degree of asymmetry, and C is a constant proportional to the total intensity. This function yielded higher-quality fits than Gaussian, Lorentzian, Pseudo-Voigt, Skewed-Gaussian, or combinations thereof.

The collapse rate of Na-MMT during ion exchange with 1 M KCl was quantified using the integrated basal spacing peak intensities $q_{001,Na\text{-}MMT} = 0.332$ Å^{-1} and $q_{001,K\text{-}MMT} = 0.400$ Å^{-1}. The fraction of Na-MMT peak intensity contributing to the total basal spacing peak intensity, $f_{19\,\text{Å}}$, was plotted as a function of the reaction time. A renormalized exponential function was fit to extract the collapse rate, a, and equilibrium ratio of Na-MMT to K-MMT, b,

$$f_{19\,\text{Å}} = \left(1 - f_{19\,\text{Å}}^{eq}\right)e^{-at} + f_{19\,\text{Å}}^{eq} \qquad (3)$$

The total particle concentration in solution was quantified using the Porod invariant, Q_v,

$$Q_v = \int_{q=0}^{\infty} q^2 I(q)dq \qquad (4)$$

Cryo-transmission electron microscopy

Suspensions of Na-MMT or K-MMT with particle concentrations of 5 mg/mL were deposited as 2-3 μL aliquots onto 300-mesh lacy carbon Cu grids (Electron Microscopy Sciences) which had been glow-discharged in air plasma for 15 seconds. For samples at a 1:2 mixing ratio of KCl:Na-MMT, 2 μL Na-MMT

was applied to the grid followed by 1 µL KCl, and the resulting drop was mixed with a pipette tip for ~1s. Excess solution was removed by automatic blotting (1 blot for 10 s, blot force 10 at 100% relative humidity) before plunge-freezing in liquid ethane using an automated vitrification system (FEI Vitrobot). Vitrified samples were loaded into the microscope using a custom-made cryo-holder held at an operating temperature of approximately −180 °C.

Imaging was performed with a Titan Krios TEM operated at 300 kV, equipped with a BIO Quantum energy filter. Images were recorded on a Gatan K2 IS direct electron detecting camera with a pixel size of 0.72 Å/pixel. Imaging was performed under cryogenic conditions using a low electron dose rate (< 10 e$^-$ Å^{-2}s^{-1}) to minimize sample damage. Automated low-dose acquisition using SerialEM software, analogous to that used for single-particle analysis of biomacromolecules, allowed for high-throughput identification particles in edge-on orientation, which were then imaged at higher magnification. This method produces particles that are randomly oriented with respect to the beam direction such that most are not aligned edge-on, where strong absorption and diffraction from clay layers produces dark contrast that is proportional to the electron density. At least 10 images were acquired at each location, and MotionCor2 software was used to correct for drift between frames before averaging frames together.

Measurements of interlayer spacing were performed using ImageJ 2.0.0 (NIH, http://rsb.info.nih.gov/ij/). Direct measurements of interlayer spacings were determined for coplanar layers. Fourier transform (FT) of the entire image region containing a particle was used to extract the average spacing by radially integrating the whole FT. Profiles for particles with only a single orientation at an angle θ, were integrated within an angular range φ. These profiles are qualitatively comparable to X-ray scattering spectra. Bragg filtering was performed by taking the FT of a region, isolating the Bragg spot(s) of interest using a binary mask to set all other pixel values to zero, and taking the inverse FT of the masked image (**Supporting Figure 5**). This technique reveals the source of Bragg features in the FT from the original image by reproducing the intensity they contribute, allowing for identification of particles within a stack (**Supporting Figure 5c**) vs. elsewhere in solution (**Supporting Figure 5e**).

6. References

1   Bergaya, F. & Lagaly, G. in *Handbook of Clay Science Developments in Clay Science* (2013).
2   Norrish, K. The Swelling of Montmorillonite. *Nature* **1**, 120-134 (1954).
3   Paineau, E. *et al.* Aqueous suspensions of natural swelling clay minerals. 1. Structure and electrostatic interactions. *Langmuir* **27**, 5562-5573, doi:10.1021/la2001255 (2011).
4   Morvan, M., Espinat, D., Lambard, J. & Zemb, T. Ultrasmall- and small-angle X-ray scattering of smectite clay suspensions. *Colloids and Surfaces A: Physicochemical and Engineering Aspects* **82**, 193-203 (1994).
5   Alt-Epping, P. *et al.* Benchmark reactive transport simulations of a column experiment in compacted bentonite with multispecies diffusion and explicit treatment of electrostatic effects. *Computational Geosciences* **19**, 535-550, doi:10.1007/s10596-014-9451-x (2014).
6   Anderson, R. L. *et al.* Clay swelling — A challenge in the oilfield. *Earth-Science Reviews* **98**, 201-216, doi:10.1016/j.earscirev.2009.11.003 (2010).
7   Bourg, I. C. & Ajo-Franklin, J. B. Clay, Water, and Salt: Controls on the Permeability of Fine-Grained Sedimentary Rocks. *Acc Chem Res* **50**, 2067-2074, doi:10.1021/acs.accounts.7b00261 (2017).
8   Srodon, J. & Eberl, D. Illite. *Reviews in Mineralogy and Geochemistry* **13**, 495 (1984).
9   Plançon, A., Besson, G., Tchoubar, C., Gaultier, J. P. & Mamy, J. Qualitative and Quantitative Study of a Structural Reorganization in Montmorillonite After Potassium Fixation. *Developments in Sedimentology* **27**, 45-54 (1979).
10   Gast, R. G. Standard Free Energies of Exchange for Alkali Metal Cations on Wyoming Bentonite. *Soil Science Society of America Proceedings* **33**, 37 (1969).
11   Eberl, D. Alkali cation selectivity and fixation by clay minerals. *Clays and Clay Minerals* **28**, 161-172 (1980).
12   Fletcher, P. & Sposito, G. The Chemical Modelling of Clay/Electrolyte Interactions for Montmorillonite. *Clay Minerals* **24**, 375-391 (1989).
13   S. Nir, D. Hirsch, J. Navrot & Banin, A. Specific Adsorptionof Lithium, Sodium, Potassium, and Strontiumto Montmorillonite: Observations and Predictions1. *Soil Science Society of America Journal* **50**, 40-45 (1968).
14   Rotenberg, B., Morel, J.-P., Marry, V., Turq, P. & Morel-Desrosiers, N. On the driving force of cation exchange in clays: Insights from combined microcalorimetry experiments and molecular simulation. *Geochimica et Cosmochimica Acta* **73**, 4034-4044, doi:10.1016/j.gca.2009.04.012 (2009).
15   Teppen, B. J. & Miller, D. M. Hydration Energy Determines Isovalent Cation Exchange Selectivity by Clay Minerals. *Soil Science Society of America Journal* **70**, doi:10.2136/sssaj2004.0212 (2006).
16   Liu, X. D. & Lu, X. C. A thermodynamic understanding of clay-swelling inhibition by potassium ions. *Angew Chem Int Ed Engl* **45**, 6300-6303, doi:10.1002/anie.200601740 (2006).
17   Sánchez-Pastor, N., Aldushin, K., Jordan, G. & Schmahl, W. W. K+–Na+ exchange in phlogopite on the scale of a single layer. *Geochimica et Cosmochimica Acta* **74**, 1954-1962, doi:10.1016/j.gca.2009.12.026 (2010).
18   Ruiz Pestana, L., Kolluri, K., Head-Gordon, T. & Lammers, L. N. Direct Exchange Mechanism for Interlayer Ions in Non-Swelling Clays. *Environ Sci Technol* **51**, 393-400, doi:10.1021/acs.est.6b04747 (2017).
19   Arndt, D., Mattei, M., Heist, C. & McGuire, A. Measurement of Swelling of Individual Smectite Tactoids In Situ Using Atomic Force Microscopy. *Clays and Clay Minerals* **65**, 92-103, doi:10.1346/ccmn.2017.064053 (2017).
20   Honorio, T., Brochard, L., Vandamme, M. & Lebee, A. Flexibility of nanolayers and stacks: implications in the nanostructuration of clays. *Soft Matter* **14**, 7354-7367, doi:10.1039/c8sm01359d (2018).

21   Weigand, S. J. & Keane, D. T. DND-CAT's new triple area detector system for simultaneous data collection at multiple length scales. *Nuclear Instruments and Methods in Physics Research Section A: Accelerators, Spectrometers, Detectors and Associated Equipment* **649**, 61-63, doi:10.1016/j.nima.2010.12.045 (2011).

22   Moore, D. M. & Robert C. Reynolds, J. *Xray diffraction and the identificaiton and analysis of clay minerals*. 2 edn, (Oxford University Press, 1997).

23   Vao-soongnern, V., Pipatpanukul, C. & Horpibulsuk, S. A combined X-ray absorption spectroscopy and molecular dynamic simulation to study the local structure potassium ion in hydrated montmorillonite. *Journal of Materials Science* **50**, 7126-7136, doi:10.1007/s10853-015-9269-5 (2015).

24   Chang, F.-R. C., Skipper, N. T. & Sposito, G. Computer Simulation of Interlayer Molecular Structure in Sodium Montmorillonite Hydrates. *Langmuir* (1995).

25   Chang, F.-R. C., Skipper, N. T. & Sposito, G. Monte Carlo and Molecular Dynamics Simulations of Electrical Double-Layer Structure in Potassium-Montmorillonite Hydrates. *Langmuir* (1998).

26   Boek, E. S., Coveney, P. V. & Skipper, N. T. Monte Carlo Molecular Modeling Studies of Hydrated Li-, Na-, and K-Smectites: Understanding the Role of Potassium as a Clay Swelling Inhibitor. *J Am Chem Soc* **117**, 12608-12617 (1995).

27   Chang, F.-R. C., Skipper, N. T. & Sposito, G. Monte Carlo and Molecular Dynamics Simulation of Electrical Double-Layer Structure in Potassium-Montmorillonite Hydrates. *Langmuir* **14**, 1201-1207 (1998).

28   Bourg, I. C. & Sposito, G. Molecular dynamics simulations of the electrical double layer on smectite surfaces contacting concentrated mixed electrolyte (NaCl-CaCl2) solutions. *J Colloid Interface Sci* **360**, 701-715, doi:10.1016/j.jcis.2011.04.063 (2011).

29   Ferrage, E. Investigation of smectite hydration properties by modeling experimental X-ray diffraction patterns: Part I. Montmorillonite hydration properties. *American Mineralogist* **90**, 1358-1374, doi:10.2138/am.2005.1776 (2005).

30   Bourg, I. C. & Sposito, G. Connecting the Molecular Scale to the Continuum Scale for Diffusion Processes in Smectite-Rich Porous Media. **Environmental Science and Technology**, 2085-2091 (2010).

31   Zheng, Y. & Zaoui, A. Temperature effects on the diffusion of water and monovalent counterions in the hydrated montmorillonite. *Physica A* **392**, 5994-6001, doi:10.1016/j.physa.2013.07.019 (2013).

32   Rotenberg, B. *et al.* Water and ions in clays: Unraveling the interlayer/micropore exchange using molecular dynamics. *Geochimica et Cosmochimica Acta* **71**, 5089, doi:10.1016/j.gca.2007.08.018 (2007).

33   Gilbert, B., Comolli, L. R., Tinnacher, R. M., Kunz, M. & Banfield, J. F. Formation and Restacking of Disordered Smectite Osmotic Hydrates. *Clays and Clay Minerals* **63**, 432-442, doi:10.1346/ccmn.2015.0630602 (2015).

34   Svensson, P. D. & Hansen, S. Combined Salt and Temperature Impact on Montmorillonite Hydration. *Clays and Clay Minerals* **61**, 328-341, doi:10.1346/ccmn.2013.0610412 (2013).

35   Bergaya, F. & Lagaly, G. *Handbook of Clay Science*. (Elsevier, 2013).

36   Tsipursky, S. I. & Drits, V. A. The distribution of octahedral cations in the 2:1 layers of dioctaheral smectites studied by oblique texture electron diffraction. *Clay Minerals* **19**, 177-193 (1984).

37   Laird, D. A. & Shang, C. Relationship between cation exchagne selectivity and crystalline swelling in expanding 2:1 phyllosilicates. *Clays and Clay Minerals* **45**, 681-689 (1997).

38   Wada, N., Hines, D. R. & Ahrenkeil, S. P. X-ray-diffraction studies of hydration transitions in Na vermiculite. *Physical Review B* **41**, 12895 (1990).

39   Silva, G. J. d., Fossum, J. O., DiMasi, E. & Måløy, K. J. Hydration transitions in a nanolayered synthetic silicate: A synchrotron x-ray scattering study. *Physical Review B* **67**, 094114, doi:10.1103/PhysRevB.67.094114 (2003).

40   Verburg, K., Baveye, P. & McBride, M. B. Cation-Exchange Hysteresis and Dynamics of Formation and Breakdown of Montmorillonite Quasi-Crystals. *Soil Science Society of America Journal* **59**, 1268-1273 (1995).

41   Tournassat, C., Bizi, M., Braibant, G. & Crouzet, C. Influence of montmorillonite tactoid size on Na–Ca cation exchange reactions. *Journal of Colloid and Interface Science* **364**, 443-454, doi:10.1016/j.jcis.2011.07.039 (2011).

42   Tambach, T. J., Bolhuis, P. G., Hensen, E. J. M. & Smit, B. Hysteresis in Clay Swelling Induced by Hydrogen Bonding: Accurate Prediction of Swelling States. *Langmuir* **22**, 1223-1234 (2006).

43   Whitley, H. D. & Smith, D. E. Free energy, energy, and entropy of swelling in Cs-, Na-, and Sr-montmorillonite clays. *J Chem Phys* **120**, 5387-5395, doi:10.1063/1.1648013 (2004).

44   Smith, D. E., Wang, Y., Chaturvedi, A. & Whitley, H. D. Molecular Simulations of the Pressure, Temperature, and Chemical Potential Dependencies of Clay Swelling. *Journal of Physical Chemistry B* **110**, 20046-20054 (2006).

45   Heinz, H., Vaia, R. A. & Farmer, B. L. Interaction energy and surface reconstruction between sheets of layered silicates. *The Journal of Chemical Physics* **124**, 1, doi:10.1063/1.2202330 (2006).

46   Oueslati, W., Rhaiem, H. B., Lanson, B. & Amara, A. B. H. Selectivity of Na–montmorillonite in relation with the concentration of bivalent cation (Cu2+, Ca2+, Ni2+) by quantitative analysis of XRD patterns. *Applied Clay Science* **42**, 224-227, doi:10.1016/j.clay.2008.09.010 (2009).

47   Michot, L. J. *et al.* Phase Diagrams of Wyoming Na-Montmorillonite Clay. Influence of Particle Anisotropy. *Langmuir* **20**, 10829-10837 (2004).

48   Ferrage, E., Lanson, B., Michot, L. J. & Robert, J.-L. Hydration Properties and Interlayer Organization of Water and Ions in Synthetic Na-Smectite with Tetrahedral Layer Charge. Part 1. Results from X-ray Diffraction Profile Modeling. *Journal of Physical Chemistry: C* **114**, 4515-4526 (2010).

49   Dazas, B. *et al.* Influence of Tetrahedral Layer Charge on the Organization of Interlayer Water and Ions in Synthetic Na-Saturated Smectites. *The Journal of Physical Chemistry C* **119**, 4158-4172, doi:10.1021/jp5123322 (2015).

50   Holmboe, M., Wold, S. & Jonsson, M. Porosity investigation of compacted bentonite using XRD profile modeling. *J Contam Hydrol* **128**, 19-32, doi:10.1016/j.jconhyd.2011.10.005 (2012).

51   S. Balme, M. Kharroubi, A. Haouzi & Henn, F. Non-Arrhenian Ionic dc Conductivity of Homoionic Alkali Exchanged Montmorillonites with Low Water Loadings. *Journal of Physical Chemistry C* **114**, 9431-9438 (2010).

52   Druger, S. Ionic transport in polymer electrolytes based on renewing environments. *Journal of Chemical Physics* **100**, 3979-3984, doi:10.1063/1.466331 (1993).

53   Toby, B. H. & Von Dreele, R. B. GSAS-II: the genesis of a modern open-source all purpose crystallography software package. *Journal of Applied Crystallography* **46**, 544-549, doi:10.1107/S0021889813003531 (2013).

54   Von Dreele, R. B. Small-angle scattering data analysis inGSAS-II. *Journal of Applied Crystallography* **47**, 1784-1789, doi:10.1107/s1600576714018366 (2014).

55   Beaucage, G. Approximations Leading to a Unified Exponential/Power-Law Approach to Small-Angle scattering. *Journal of Applied Crystallography* **28**, 717-728 (1995).

56   Segad, M. *et al.* Microstructural and Swelling Properties of Ca and Na Montmorillonite: (In Situ) Observations with Cryo-TEM and SAXS. *The Journal of Physical Chemistry C* **116**, 7596-7601, doi:10.1021/jp300531y (2012).

57   Tester, C. C., Aloni, S., Gilbert, B. & Banfield, J. F. Short- and Long-Range Attractive Forces That Influence the Structure of Montmorillonite Osmotic Hydrates. *Langmuir* **32**, 12039-12046, doi:10.1021/acs.langmuir.6b03265 (2016).